Experimental Thermal and Fluid Science 112 (2020) 109986

Contents lists available at ScienceDirect

Experimental Thermal and Fluid Science

journal homepage: www.elsevier.com/locate/etfs

On unsteady velocity measurements and profiling in compression waves in an asymmetrical trapezoidal channel

Ramith Fernando, Xinqian Leng, Hubert Chanson*

The University of Queensland, School of Civil Engineering, Brisbane, QLD 4072, Australia

ARTICLE INFO

Keywords:
Compression waves
Unsteady turbulence
Trapezoidal canal
Secondary currents

ABSTRACT

A compression wave is a highly-unsteady rapidly-varied free-surface flow associated with a sudden rise in water surface elevation and may travel over very long distances along flat prismatic canals. New experiments were conducted to investigate the unsteady turbulent characteristics of compression waves, in a large-size channel. The focus was on the effects of the asymmetrical trapezoidal shape of the channel cross-section on the transient turbulence characteristics of the three-dimensional compression wave. The measurements showed a complicated unsteady motion down the transverse slope, underneath the leading edge of the compression wave. A marked increase in free-surface elevation was observed during the surge passage. A three-dimensional transient motion was observed. An intense transient recirculation was seen next to the invert at the base of the transverse slope and in the shallow flow zones. Visual observations and velocity measurements showed some recirculation primarily in the shallow water region. The results highlighted strong secondary currents on the transverse slope, albeit for short, transient periods.

1. Introduction

In an open channel, a compression wave is a highly-unsteady rapidly-varied free-surface flow associated with a sudden rise in water surface elevation [27]. A compression wave can travel over very long distances along flat prismatic canals, because it can absorb random disturbances on both sides of the front, making the compression wave stable and self-perpetuating [13,11]. Large-scale industrial applications encompass rejection and load acceptance surges in hydro-power canals following rapid turbine start or stoppage, surges in water supply systems following rapid gate operation, and operation of lock gates in navigation canals [8,28]. Basic one-dimensional modelling may predict successfully the propagation of a compression wave [24,21], but does not provide any information on the unsteady turbulence and three-dimensional hydrodynamic transient flows, for example during incidents leading to operational restrictions [9,30].

Recently, physical and numerical CFD studies of compression waves were undertaken in rectangular channels. All the data showed a rapid deceleration during the passage of the compression wave followed by some transient recirculation underneath the wave front [12,6,17]. The effect of transient recirculation, and associated large vortical structures, were linked to secondary flows. Only a few investigations were conducted in non-rectangular flumes, including some free-surface observations in symmetrical trapezoidal channels, and more recently velocity measurements in an asymmetrical trapezoidal canal [15] (Table 1).

In this study, new experiments were conducted to investigate the unsteady turbulent characteristics of compression waves in an asymmetrical trapezoidal canal. They were performed in a systematic manner under controlled flow conditions, with detailed free-surface and velocity measurements in a large-size channel. The study focused on the unsteady turbulence characteristics of the three-dimensional compression wave. Using acoustic Doppler velocimetry and profiling, the turbulent transient recirculation and secondary motion were characterised. The measurements showed a complicated unsteady motion down the transverse slope during the passage of the compression wave front.

2. Experimental methods, facility and instrumentation

2.1. Experimental channel and instrumentation

The experiments were conducted in a 19 m long, 0.7 m wide channel (Fig. 1A). The bed was made from PVC and the 0.52 m high sidewalls were made of glass. The trapezoidal cross section was modelled with a 0.14 m high 1V:3H transverse slope (Fig. 1B),

* Corresponding author.
E-mail address: h.chanson@uq.edu.au (H. Chanson).

https://doi.org/10.1016/j.expthermflusci.2019.109986
Received 20 April 2019; Received in revised form 29 October 2019; Accepted 5 November 2019
Available online 07 November 2019

Table 1
Experimental investigations of compression waves in trapezoidal channels.

Reference	S_o	Q (m^3/s)	d_1 (m)	Fr_1	Channel geometry	Measurement(s)
Sandover and Taylor [26]	–	–	–	–	Symmetrical trapezoidal cross-section. L = 18.3 m, W_2 = 0.305 m, λ = 0.58, 1.0, 1.73	Free-surface data and compression wave celerity
Benet and Cunge [1]	0.0036	0 to 0.006	0.057 to 0.14	1 to 1.33	Symmetrical trapezoidal cross-section. L = 32.5 m, W_1 = 0.172 m, λ = 2	Free-surface data and compression wave celerity
	0.0001 to 0.00015	130 to 235	6.4 to 9.16	1.07 to 1.16	Symmetrical trapezoidal cross-section. L = 11,262 m, W_1 = 9.0 m, λ = 2 (*)	
	–	270 to 300	7.53 to 6.19	1.06 to 1.15	Symmetrical trapezoidal cross-section. L = 17,740 m, W_1 = 8.6 m, λ = 2 (*)	
Treske [30]	0.00017	–	–	1.05 to 1.28	Symmetrical trapezoidal cross-section. L = 100 m, W_1 = 1.0 m, λ = 1	Free-surface data and compression wave celerity
	0	–	0.040 to 0.160	1.02 to 1.28	Symmetrical trapezoidal cross-section. L = 130 m, W_1 = 1.24 m, λ = 3	
Kiri et al. [15]	0.002216	0.030 to 0.100	0.13 to 0.21	1.3 to 1.8	Asymmetrical trapezoidal cross-section. L = 19 m, W_2 = 0.70 m, W_1 = 0, λ = 5, D = 0.140 m	Free-surface data and unsteady velocity measurements
Present study	0.002216	0.006 to 0.100	0.10 to 0.22	1 to 1.6	Asymmetrical trapezoidal cross-section. L = 19 m, W_2 = 0.70 m, W_1 = 0.280 m, λ = 3, D = 0.140 m	Free-surface data and unsteady ADV/Profiler velocity measurements

Notes: D: transverse bed elevation difference; L: test section length; S_o: longitudinal bed slope; W_1: bottom width; W_2: maximum channel width; λ: transverse slope inverse value (Fig. 1); (–): data not available; (*): field observations.

manufactured in PVC and installed between 1.25 m < x < 17.2 m, with x the longitudinal distance from the upstream end of the glass sidewall channel. At the downstream end of the channel, a custom made Tainter gate was installed at x = 18.1 m (Fig. 1A). The rapid gate closure was used to generate the compression wave. Fig. 1 shows a sketch of the facility and Fig. 2 presents photographs of the compression wave. Fig. 2A, B and C illustrate the surge propagation in the experimental channel. The geometry of the channel was selected for two applications. The asymmetrical cross-sectional shape may correspond to natural systems affected by a compression wave: e.g., a river channel subjected to a dam break wave. Such natural channels have typically an asymmetrical shape. Second, using a method of images, the current configuration might be seen as a half section of a man-made trapezoidal channel, with 1V:3H side slopes, e.g. used for water supply canals and hydropower systems.

A rail mounted pointer gauge was used to measure the free-surface elevation in steady flows. Steady velocity measurements were performed using a Dwyer® 166 Series Prandtl Pitot tube (∅ = 3.18 mm), to check the validity of the acoustic Doppler velocimeter and Profiler data, in the steady-state flow conditions. In steady flows, the Prandtl-Pitot tube was also calibrated to provide the boundary shear stress with the tube lying on the boundary, acting as a Preston tube [2].

Ten non-intrusive Microsonic™ Mic +25/IU/TC acoustic displacement meters (ADMs) were used to measure the unsteady free-surface elevations. The ADMs were positioned at x = 6.96 m, 8.6 m, 10.96 m, 17.41 m and 18.17 m. At x = 8.6 m, six ADMs recorded simultaneously the shape of the bore at six transverse locations (y = 0.1–0.6 m) as seen in Fig. 2D and 2E, with y the transverse distance from the right sidewall. The ADMs were sampled simultaneously and synchronously with and at the same sampling frequency as the velocimeter, i.e. 100 Hz and 200 Hz with the Profiler and ADV respectively.

Unsteady velocity measurements were conducted using acoustic Doppler velocimetry at x = 8.6 m. A Nortek™ acoustic Doppler velocimeter Vectrino II Profiler (Profiler) (Serial number P27338, Hardware ID VNO 1366) was used to record simultaneously 30 velocity measurements, from $z\text{-}z_{bed} = 0$ (i.e. base of the bed) up to $z\text{-}z_{bed} = 0.029$ every 1 mm. The Profiler was sampled at 100 Hz. A Nortek™ acoustic Doppler velocimeter (ADV) Vectrino+ (Serial No. VNO 0436) was used for point measurements, with a sampling volume 0.050 m away from the emitter and 0.0058 m above the base of the emitter. The side-looking ADV was sampled at 200 Hz and used to characterise accurately the unsteady Reynolds stresses.

While the Profiler signal output is known for the existence of outlier data [7,19,29], neither the Profiler nor the ADV signal outputs were despiked during unsteady flow conditions, and the raw data were used directly for analysis following Leng and Chanson [19]. Although a number of studies detailed various ADV signal post-processing methods, all were developed and validated in steady flows only. In highly unsteady rapidly-varied flow conditions, these post-processing techniques are not applicable (e.g. Nikora, 2004, Personal Communication) [16].

2.1.1. Experimental uncertainties and errors

In steady flows, the water depths were measured with pointer gauges with an accuracy of ± 0.5 mm. In unsteady flows, the water depths were recorded with acoustic displacement meters calibrated against the pointer gauges. The error on the unsteady water depth data was expected to be within ± 0.5 mm. Three velocity measurement systems were used: a Prandtl Pitot tube, an ADV Vectrino+, and a Vectrino II Profiler. In steady flows, all the velocity measurements were similar within 2%. They were further checked in terms of conservation of mass against discharge measurements using a magneto flow meter. The results showed a deviation within 2–3% with the discharge measurements.

During the unsteady experiments, the high level of repeatability of the experiments and fast sampling rate enabled to synchronise the data within ± 0.05 s.

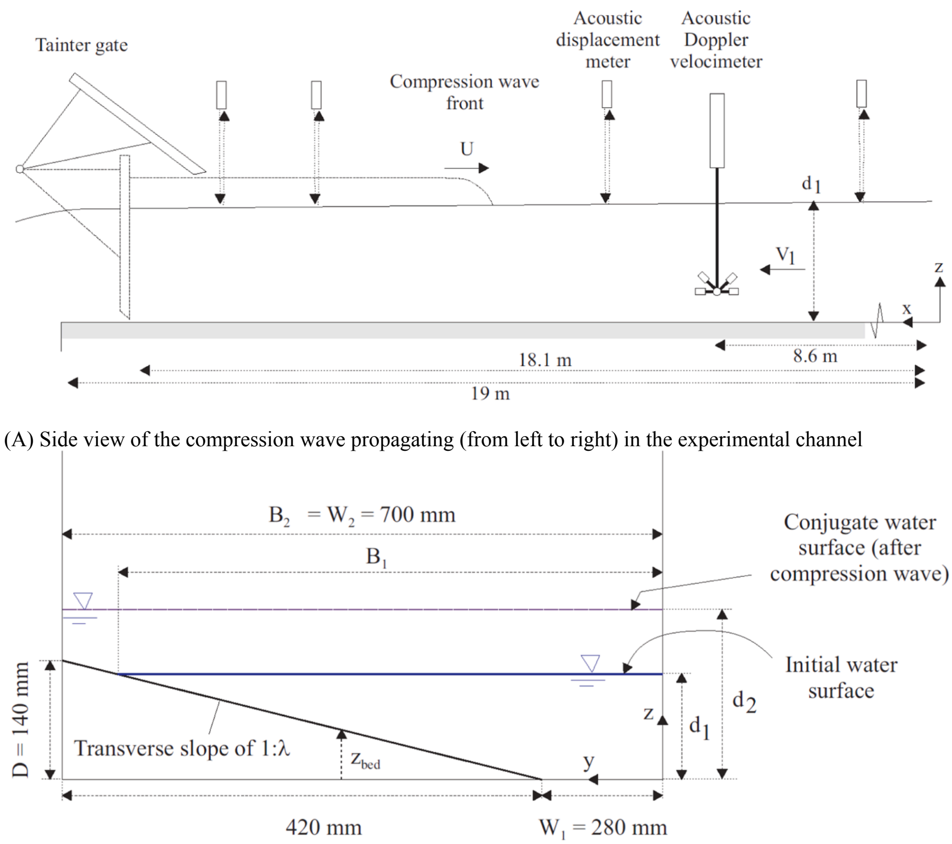

(A) Side view of the compression wave propagating (from left to right) in the experimental channel

(B) Undistorted transverse cross-section looking downstream

Fig. 1. Definition sketch of a compression wave in an asymmetrical trapezoidal channel.

2.2. Steady flow conditions

Steady flow observations were conducted for discharges ranging from 0.006 m^3/s to 0.100 m^3/s. The open channel flow was at uniform equilibrium, i.e. normal flow conditions, along most of the flume length. The free-surface flow was subcritical, i.e. the water depth was greater than the critical flow depth. Calculations of the critical flow depth for a trapezoidal channel are detailed in Appendix A. Further the water surface was horizontal in the transverse direction.

The velocity measurements indicated that the flow was three-dimensional, because of the asymmetrical cross sectional shape. The velocities typically decreased in shallow water depths and all the observations indicated a faster flow towards the deeper section of the channel (Fig. 3A). The boundary shear stress distribution was not uniform along the wetted perimeter. This is illustrated in Fig. 3C, with Fig. 3B presenting the definition of the perimetric coordinate Y, measured along the wetted perimeter, with Y = 0 at the bottom right corner (y = 0, z = 0). Large variations were observed along both the sidewalls, bottom invert and inclined transverse slope. Minimum boundary shear stress was observed at the corners in steady flows. The minimum was linked to the occurrence of secondary flow cells on each side of the corner bisector, and local turbulent losses [10,22]. Typical experimental results are shown in Fig. 3C, where the horizontal axis is the dimensionless perimetric distance Y/W_1, with W_1 the horizontal invert width (Figs. 1B & 3B). In Fig. 3C, the vertical thick solid lines correspond to the bottom right corner Y = 0 at (y = 0, z = 0) and to the edges of the inclined transverse slope.

2.3. Unsteady flow conditions

This study focused on compression waves in translation, for which the mean characteristics were independent of the generation process. The main sampling location (x = 8.6 m) was selected accordingly. For each experiment, the compression wave was generated by the rapid closure of the downstream Tainter gate and the compression wave front propagated upstream (Fig. 2).

Visual observations and free-surface measurements were undertaken for initial discharges Q ranging from 0.006 m^3/s to 0.100 m^3/s (Table 1). Different gate openings were used to alter the bore celerity and thereby the Froude number. Detailed velocity measurements were conducted for three discharges (Q = 0.0026, 0.054 and 0.094 m^3/s) (Table 2). Table 2 summarises the experimental flow conditions, where Q is the initial steady water discharge, d_1 is the initial water depth, h is the Tainter gate opening after closure, U is the compression wave celerity positive upstream, y is the transverse distance from the right sidewall, z is the vertical elevation, z_{bed} is the local bed elevation (Fig. 1) and Fr_1 is the compression wave Froude number defined as:

$$Fr_1 = \frac{U+V_1}{\sqrt{g\times\frac{A_1}{B_1}}} \tag{1}$$

with V_1 the initial flow velocity, g the gravity acceleration, A_1 and B_1 the initial flow cross-section area and free-surface width respectively. Velocity data with the Profiler were obtained at various transverse locations close to the bed: $z-z_{bed} = 0$ to 0.029 m. These were complemented by data collected with the ADV.

All velocity measurement experiments were repeated 25 times and ensemble-averaged, following Chanson and Docherty [5] and Leng and Chanson [18]. The median free-surface elevations and velocity components were calculated from the total ensemble, as well as the fluctuating properties.

Finally the unsteady flow motion is a free-surface flow, for whcih the gravity effects are important. Any upscaling of the results must be based upon a Froude similitude [1,11].

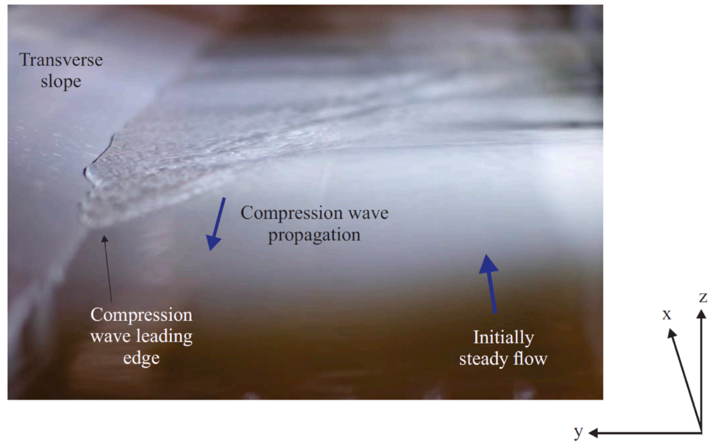

(A) Q = 0.0063 m^3/s, Fr_1 = 1.3 - Details of wave front along transverse slope looking downstream (see Fig. 1B for coordinate system)

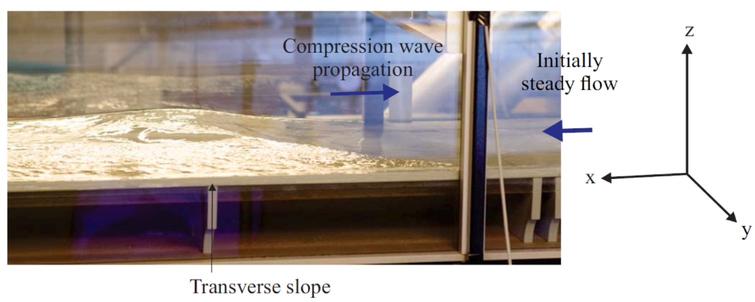

(B) Q = 0.026 m^3/s, d_1 = 0.105 m, U = 0.67 m/s, Fr_1 = 1.34 - Sideview with compression wave propagating from left to right (arrow)

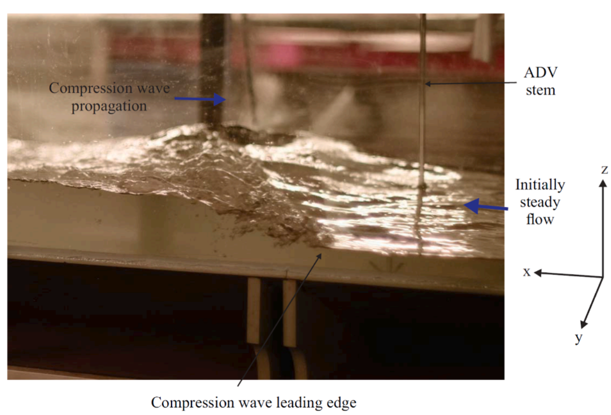

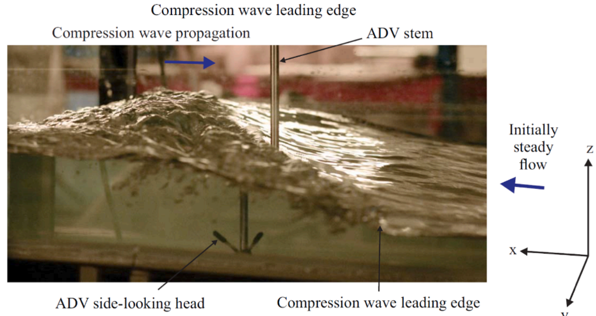

(C) Q = 0.054 m^3/s, d_1 = 0.15 m, U = 0.83 m/s Fr_1 = 1.4, x = 8.6 m - Sideviews with compression wave propagating from left to right (note the ADV stem and submerged ADV side-looking head)

Fig. 2. Photographs of compression wave propagation in the asymmetrical trapezoidal channel - Flow conditions are listed in the figure sub-caption, including the initial discharge Q, initial water depth d_1, compression wave celerity U, compression wave Froude number Fr_1, and longitudinal distance x.

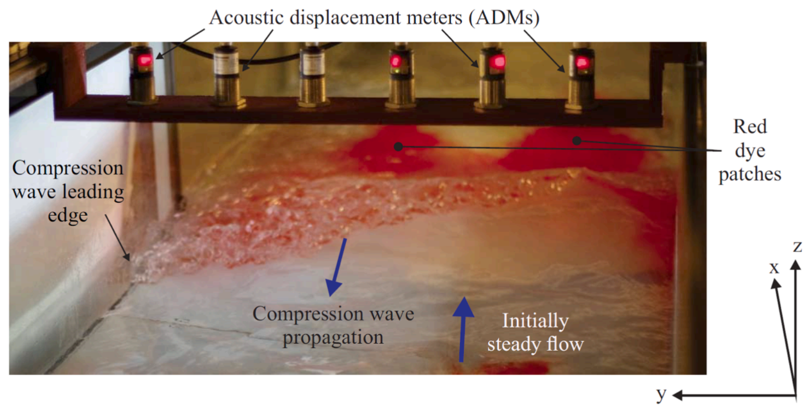

(D) Q = 0.054 m^3/s, d_1 = 0.15 m, U = 0.71 m/s Fr_1 = 1.24, x = 8.6 m, with dye injection, looking downstream

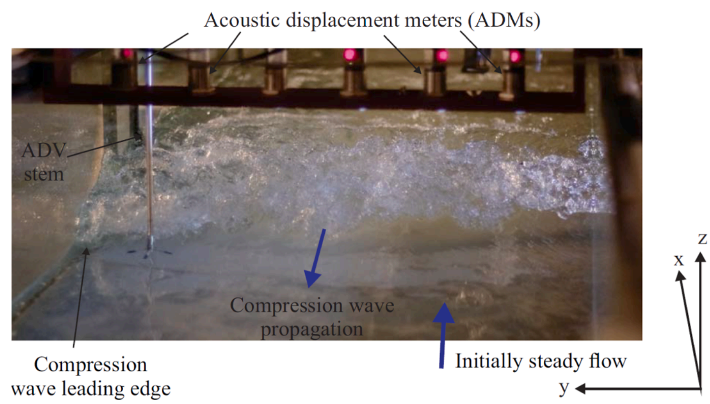

(E) Q = 0.094 m^3/s, d_1 = 0.205 m, U = 1.06 m/s, Fr_1 = 1.35, x = 8.6 m, looking downstream - Note the ADV Profiler stem next to the left sidewall

Fig. 2. (*continued*)

3. Basic flow patterns

Visual observations were undertaken for a range of initial flow conditions, with initial depths d_1 measured next to the right sidewall (Table 1). Fig. 2 presents several photographs, with the details of flow conditions listed in the figure caption, while Appendix B lists a number of video movies available in the Digital Appendix (Supplementary material). Altogether, a number of unsteady compression wave patterns were observed at x = 8.6 m, depending upon the compression wave Froude number Fr_1 and relative initial flow depth d_1/D, with D being the maximum height of the transverse bed slope (D = 0.140 m, Fig. 1). For $d_1/D < 1$, the initial free-surface width B_1 was less than the full canal width B = 0.70 m, as sketched in Fig. 1. Such an initial flow condition, i.e. $d_1/D < 1$, is seen in Fig. 2A and B, and viewed in Movie CIMG5228.MOV (Appendix B). As the compression wave propagated upstream, it expanded over the transverse slope as illustrated in Fig. 2A and CIMG5228.MOV (Appendix B); then the new (conjugate) free-surface width was greater than the initial one. For $d_1/D > 1$, the initial and conjugate free-surface breadths were identical ($B_1 = B_2 = B = 0.70$ m). This initial condition, i.e. $d_1/D > 1$, is illustrated in Fig. 2C, D and E, and in Movie CIMG5121.MOV (Appendix B). The propagation of the compression wave did not yield any change in free-surface width, as viewed in the Movie CIMG5121.MOV (Appendix B).

For all flow conditions, a key feature was the three-dimensional shape of the compression wave front. For the present experimental conditions (Table 1), the compression wave was typically breaking in shallow water next to the left side, while strong secondary waves followed the wave front in deep waters towards the right sidewall (Movies CIMG5121.MOV and CIMG5228.MOV, Appendix B). The compression wave front propagated upstream with an angle to the left sidewall less than 90° (Fig. 2 and Movies), although the celerity of the compression wave was the same across the channel. The leading edge of the compression wave arrived first at the sampling location in the shallow water section. Note that, for the present flow conditions, the compression wave surface rose past the upper end of the transverse slope: i.e., the conjugate free-surface width was $B_2 = W_2 = 0.70$ m. Slow motion videos (Appendix B) outlined an increased level of level of asymmetry of the wave front with reduced flow rates.

Dye-injection tests showed a transient recirculation zone about $0.29 < y/B < 0.57$. This transient recirculation zone was observed with the dye travelling downstream towards the front of the compression wave, and then changing direction immediately after the wave front between $0.29 < y/W < 0.57$. The compression wave front was observed to trap the dye for higher flow rates. After the dye reached the front, the dye remained entrapped in the roller before slowly moving downstream. Earlier dye injection tests by KIRI, et al. [15] showed a different, more contrasted dye dispersion pattern at the surge front, about $y/W \approx 0.5$–0.6. Such an effect was captured, although not as significantly, in the current study.

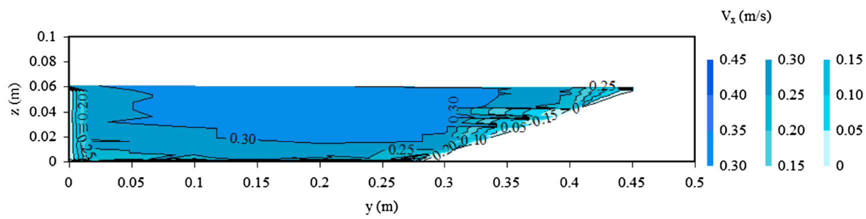

(A) Longitudinal velocity contour map for Q = 0.0063 m^3/s and d_1 = 0.061 m

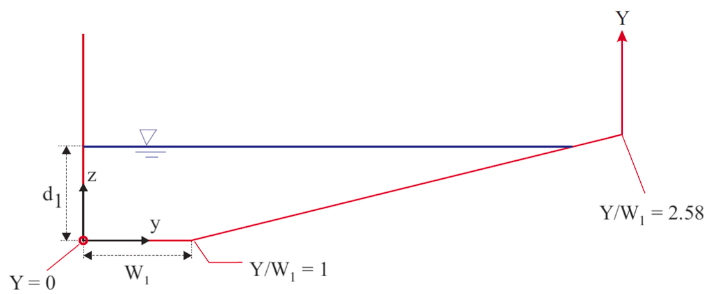

(B) Definition sketch of the perimetric coordinate Y (red axis), looking upstream

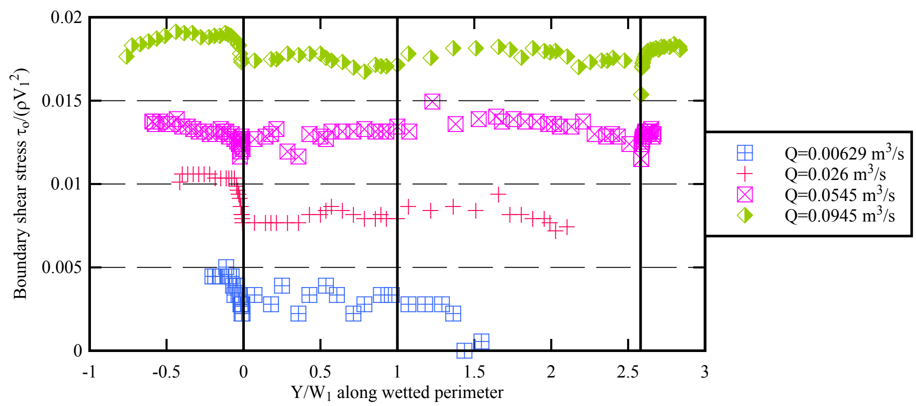

(C) Transverse distributions of dimensionless boundary shear stress as a function of the dimensionless perimetric coordinate - Y = 0 at bottom left corner of channel and Y < 0 along the right sidewall (Fig. 3B), with the bottom corners drawn as thick vertical lines - Data were offset vertically by +0.005 (Q = 0.026 m^3/s), +0.010 (Q = 0.054 m^3/s), and +0.015 (Q = 0.094 m^3/s)

Fig. 3. Steady flow velocity and boundary shear stress in the asymmetrical trapezoidal channel under steady flow conditions.

Free-surface measurements showed the three-dimensional nature of the compression waves. Fig. 4 presents typical dimensionless time-series of ensemble-averaged free-surface data at x = 8.6 m and two transverse locations y. The experiments were repeated 25 times and ensemble-averaged in terms of the median surface elevation. Prior to the arrival of the compression wave, i.e. $t.(g.B_1/A_1)^{1/2} < 680$ in Fig. 4, the water depth was constant in the initially steady flow. The arrival of the compression wave was associated with a rapid increase in water depth, seen in Fig. 4 about $t\cdot(g\cdot B_1/A_1)^{1/2} < 700$–710.

Three-dimensional free-surface profiles generated from the interpolation of the six ADMs installed at x = 8.6 m between y = 0.1 m and y = 0.6 m, spaced 0.1 m apart. Fig. 5 presents data for two flow rates highlighting the unsteady free-surface flow asymmetry. Note that Fig. 5A corresponds to the same flow conditions as for Fig. 2A and B.

Overall the present results showed a number of common features with compression wave propagation in a compound flume [23] and in an asymmetrical canal [15], as well as with field observations of tidal bores in natural channels, e.g. in the Arcins Channel of the Garonne River, France [4,14,25].

4. Free-surface and velocity measurements

The compression wave was generated by the rapid gate closure at the downstream end of the channel. The water piled up against the closed gate leading to the wave formation and its upstream translation. Initially the shape of the compression wave evolved with time in response to the non-rectangular channel cross-section as well as the rapid change in wetted area and channel shape during the generation and initial acceleration phases. As the compression wave propagated further upstream, i.e. x < 14 m, its shape evolved more gradually with time,

Table 2
Experimental flow conditions for ensemble-averaged velocity measurements in a compression wave propagating upstream in an asymmetrical trapezoidal channel (Present study).

Ref.	Q (m^3/s)	d_1 (m) ([1])	h (m)	U (m/s) ([1])	Fr_1 ([1])	Velocimeter	x (m)	y (m)	$z\text{-}z_{bed}$ (m)
Q26a	0.026	0.102	0	0.67	1.31	Profiler	8.6	0.1, 0.2 & 0.3	0 to 0.029
			0.025	0.50	1.11				
Q54a	0.054	0.15	0	0.83	1.4	Profiler		0.1, 0.2, 0.3, 0.4 & 0.5	
			0.030	0.71	1.24				
Q94a	0.094	0.205	0	1.06	1.35	Profiler		0.1, 0.2, 0.3, 0.4, 0.5 & 0.6	
			0.015	1.05	1.33	Profiler		0.6	
			0.065	0.84	1.11	Profiler		0.1, 0.2, 0.3, 0.4, 0.5 & 0.6	
Q26b	0.026	0.103	0	0.67	1.32	ADV	8.6	0.2	0.0058–0.078
								0.26	0.0058–0.055
								0.28	0.0058–0.055
								0.3	0.0058–0.071
								0.4	0.0058–0.0374
								0.5	0.0058
Q54b	0.054	0.0151	0	0.83	1.4	ADV		0.2	0.0058–0.1125
								0.26	0.012–0.024
								0.28	0.012–0.024
								0.3	0.0058–0.1058
								0.4	0.0058–0.0725
								0.5	0.0058–0.0391
								0.6	0.0058

Notes: d_1: initial water depth; h: Tainter gate undershoot opening after closure; Fr_1: Froude number of compression wave; Q: initially steady water discharge; U: compression wave celerity; y: transverse distance from right sidewall; z_{bed}; bed elevation at the transverse location y; ([1]): measured at x = 8.6 m.

and became nearly unchanged at the observation point x = 8.6 m. There, Fig. 5 presents typical time-variations of the two-dimensional water depth during the propagation of the surge. Fig. 5A corresponds to a mostly-undular bore for an initially-small discharge with $d_1/D < 1$, showing a three-dimensional surface shape, consistent with the free-surface photographs and movies (e.g. Fig. 2B and movie CIMG5228.MOV (Appendix B)). Fig. 5B shows the variation with time of the two-dimensional water depth during a breaking bore. The results illustrated a steep sharp front, similar to visual observations in Fig. 2D and movie CIMG5141.MOV (Appendix B).

The free-surface elevation rose very rapidly during the wave passage at x = 8.6 m, and the free-surface became very turbulent. Instantaneous free-surface elevation and velocity measurements were recorded synchronously at relatively high frequency (100 and 200 Hz for the Profiler and ADV respectively). Fig. 6 shows typical time-series of the water depth, instantaneous ensemble median longitudinal velocity component V_x and its instantaneous fluctuations (V_{75}-V_{25}) for a breaking surge with undulations, in terms of the instantaneous water surface elevation z and longitudinal velocity component V_x, positive downstream, at different transverse locations y. In Fig. 6, the data are ensemble-averaged and z is the free-surface elevation above the lowest bed elevation. The curves include the ensemble-median data and, in Fig. 6A, the differences between third and first quartiles. The latter may be considered as a proxy of the instantaneous fluctuation. With the arrival of the

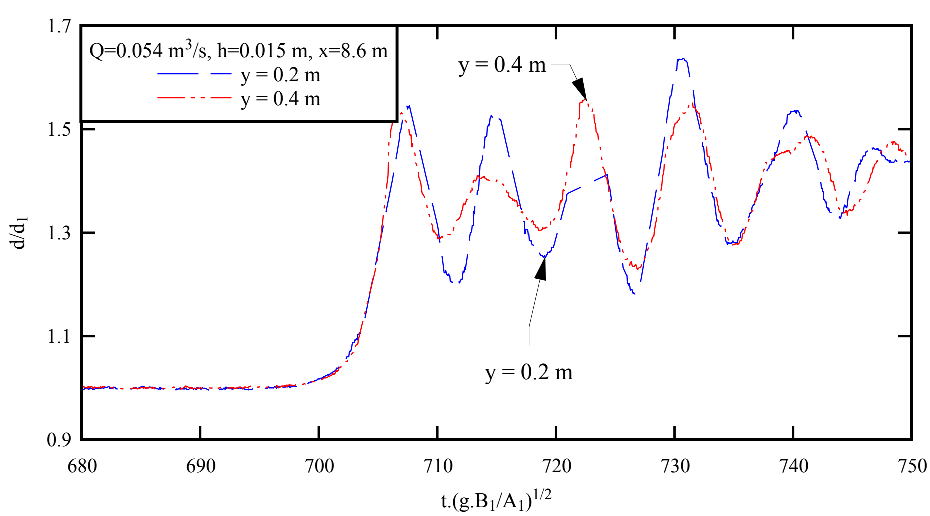

Fig. 4. Dimensionless time-variations of ensemble-median water depth during the propagation of a compression wave - Flow conditions: Q = 0.054 m^3/s, d_1 = 0.151 m, Fr_1 = 1.4, A_1 = 0.0767 m^2, B_1 = 0.70 m, x = 8.6 m, transverse locations: y = 0.2 m and 0.4 m.

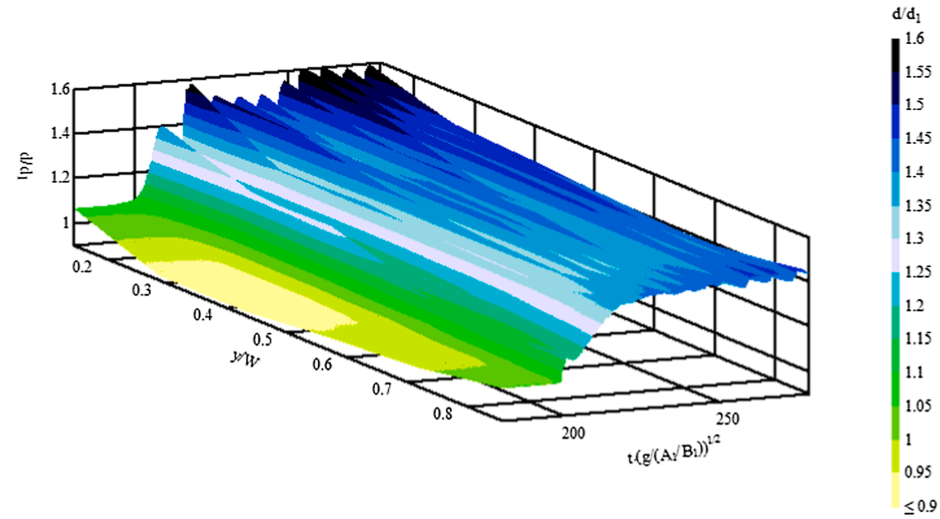

(A) $Q = 0.026$ m^3/s, $d_1 = 0.102$ m, $Fr_1 = 1.3$, $A_1 = 0.0466$ m^2, $B_1 = 0.598$ m

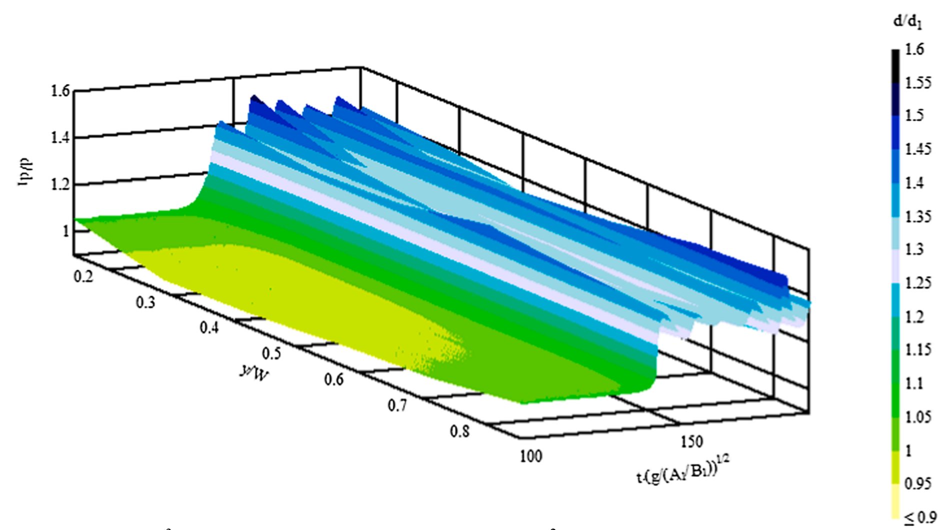

(B) $Q = 0.054$ m^3/s, $d_1 = 0.151$ m, $Fr_1 = 1.3$, $A_1 = 0.0767$ m^2, $B_1 = 0.70$ m

Fig. 5. Dimensionless time-variations of the two-dimensional ensemble-median water depth during the propagation of a compression wave.

compression wave, i.e. $t(g{\cdot}B_1/A_1)^{1/2} < 805$ (Fig. 6A) or 645 (Fig. 6B), the longitudinal velocity data showed a very brutal deceleration, followed by relatively large fluctuations of the velocity.

All the free-surface data showed that the compression wave was three-dimensional (Figs. 4–6). It was typically breaking in the shallow water side and undular in the deep-water side. Prior to the compression wave passage, the current velocity was positive downstream at all transverse locations and vertical elevations. The wave propagation had a marked effect on the velocity field, as seen in Fig. 6A and B. Key features encompassed a brutal flow deceleration as well as fast fluctuations of each velocity component during and behind the compression wave front. The present observations were consistent with earlier observations in rectangular channels [16,18], although a key feature was the three-dimensional nature of the compression wave front and associated velocity field.

Video movies were produced from the contour plots of the instantaneous ensemble-median velocity components, measured with the ADV and Profiler combined (Appendix C). In each movie, the instantaneous median free-surface elevation is shown with purple crosses and line, and the movie are replayed at 1/8th speed of real-time. Fig. 7 presents instantaneous snap shots of three movies. During the compression wave passage, the longitudinal velocity data showed a very rapid deceleration throughout the entire cross-section area, becoming negative for $0.43 < y/W < 0.71$ and a relative elevation above the bed $(z\text{-}z_0)/d_1 < 0.1$ (Appendix C, movies 26_0_Unsteady_Vx_Rev2.avi & 54_0_Unsteady_Vx_Rev3.avi). This transient recirculation zone changed size and location, with the free-surface elevation. The transverse velocity component oscillated about zero for $0.43 < y/W < 0.71$ and a relative elevation above the bed $(z\text{-}z_0)/d_1 < 0.1$ (Appendix C, movies 26_0_Unsteady_Vy_Rev2.avi & 54_0_Unsteady_Vy_Rev3.avi). In the deep section near the right sidewall, the transient secondary motion was larger in size, than in the shallower zone, and varied in size, and it appeared to change at a faster rate than in the shallow zone. The distinct secondary motion zones, either side of

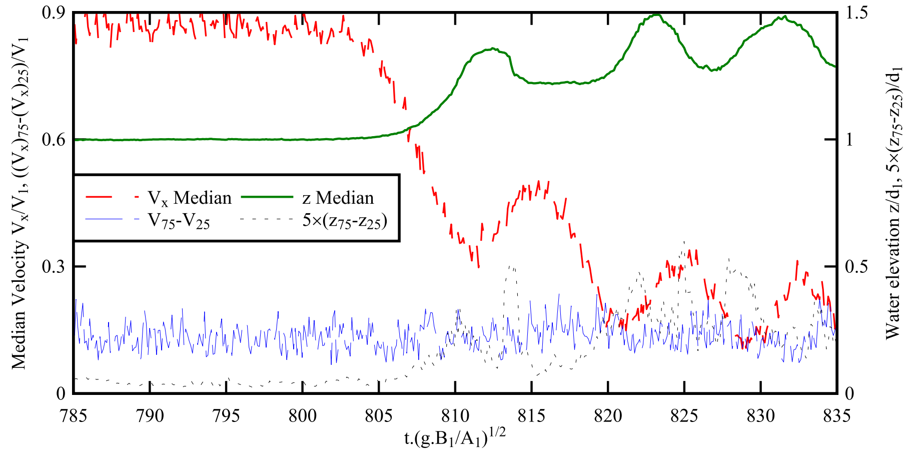

(A) Q = 0.026 m^3/s, h = 0, Fr$_1$ = 1.3, d$_1$ = 0.102 m, A$_1$ = 0.0466 m^2, B$_1$ = 0.598 m, y = 0.28 m, z$_{ADV}$ = 0.055 m

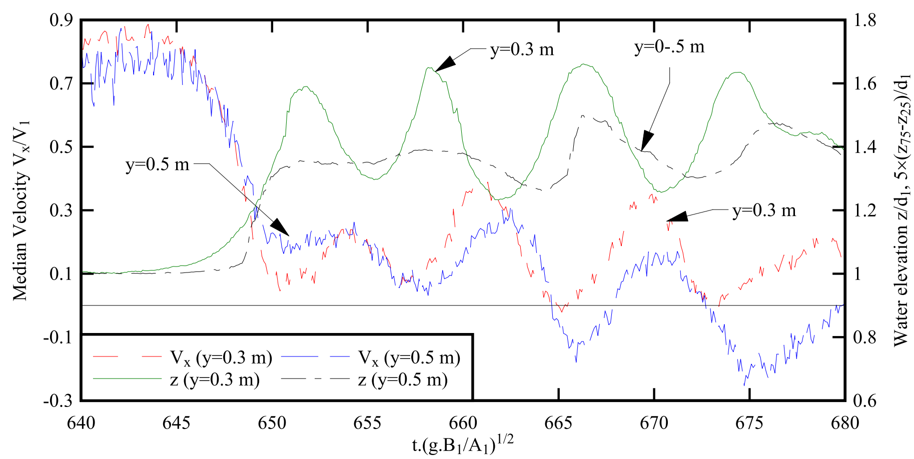

(B) Q = 0.054 m^3/s, h = 0, Fr$_1$ = 1.4, d$_1$ = 0.150 m, A$_1$ = 0.0767 m^2, B$_1$ = 0.70 m, y = 0.3 m & 0.5 m, z$_{ADV}$ = 0.1125 m

Fig. 6. Dimensionless time-variations of ensemble-median longitudinal velocity V_x and water surface elevation - ADV data at x = 8.6 m.

the boundary between transverse slopes (y/W = 0.43), might have induced some transient vertical circulation, acting as some form of instantaneous vertical shear region (Appendix B, movies 26_0_Unsteady_Vz_Rev2.avi & 54_0_Unsteady_Vz_Rev3.avi).

5. Velocity fluctuations and Reynolds stresses

The instantaneous velocity fluctuations were defined as the difference between the 75th and 25th percentiles of the ensemble. The velocity fluctuations were related to the turbulence and energy levels within flow. Maximum fluctuations would characterise times and locations where the greatest levels of turbulent mixing occurred. Typical results are presented in Fig. 8 next to the bed. All the velocity components presented large fluctuations after the passage of the compression waves, with fluctuation magnitudes comparable to the residual velocity magnitude after the wave passage. The data showed also a marked increase in longitudinal velocity fluctuations during the flow deceleration, corresponding to the passage of the compression wave (Fig. 8A).

The instantaneous Reynolds stress tensor is defined as:

$$\|\tau\| = \rho \times \begin{bmatrix} v_x \\ v_y \\ v_z \end{bmatrix} \times \begin{bmatrix} v_x & v_y & v_z \end{bmatrix} = \begin{bmatrix} \tau_{xx} & \tau_{xy} & \tau_{xz} \\ \tau_{yx} & \tau_{yy} & \tau_{yz} \\ \tau_{zx} & \tau_{zy} & \tau_{zz} \end{bmatrix} \quad (2)$$

where v is the instantaneous velocity component fluctuation, calculated as:

$$v = V - \bar{V} \quad (3)$$

with V the instantaneous velocity measurement and $\bar{V}$ the ensemble-median velocity. In the following paragraphs, the ensemble-median Reynolds stress data are presented. Since the instantaneous velocity data presented large fluctuations (Fig. 8), the instantaneous turbulent stresses similarly showed large and rapid fluctuations during and shortly after the passage of the compression wave. This is illustrated in Fig. 9, presenting the time-variation of ensemble-median turbulent stress data. The passage of the compression wave was characterised by a sudden increase in median normal stresses (Fig. 9A) and rapid oscillations of the tangential stresses (Fig. 9B). The data showed further that

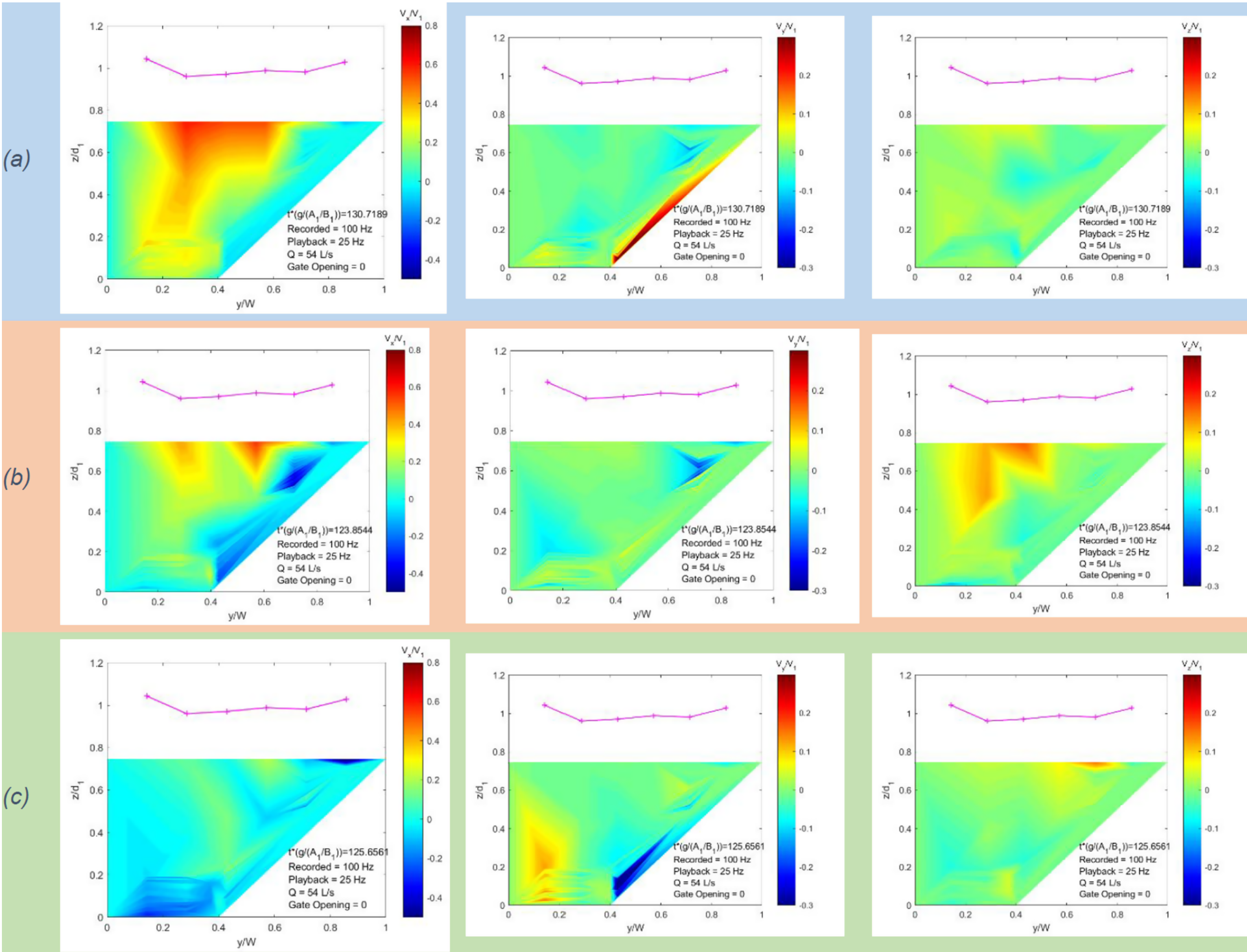

Fig. 7. Instantaneous velocity contour maps before and during a compression wave in the trapezoidal channel - Flow conditions: $Q = 0.054\ m^3/s$, $h = 0.0\ m$, $Fr_1 = 1.4$, $d_1 = 0.151\ m$. (a) Arrival of compression wave (b) Deceleration phase (c) Shortly after compression wave passage, (LEFT) V_x (MIDDLE) V_y (RIGHT) V_z.

the time lags between wave passage and large turbulent stresses was about the same irrespective of the position within the cross section. These findings were consistently observed within the entire cross-section area, although it is acknowledged that the measurements were conducted in the initially clear-water column, i.e. $z/d_1 < 1$.

6. Conclusion

This investigation assessed the instantaneous free-surface elevations and velocity fields in a compression wave propagating in an asymmetrical trapezoidal channel, to understand the three-dimensional turbulent flow and mixing processes. Physical experiments were conducted in a relatively large laboratory flume (19 m long, 0.7 m wide), modelling a half trapezoidal channel, with a 1V:3H transverse slope, alongside a flat transverse bed (0.28 m wide). The experiments were repeated 25 times and ensemble averaged.

Undular bores and breaking bores with secondary undulations were observed. A marked increase in free-surface elevation was observed during the surge passage. This was associated with a drastic deceleration of the flow. Some three-dimensional transient flow motion was observed in this investigation, linked to the asymmetry of the cross-section. There was a close correlation between velocity oscillations and free-surface undulations, in line with the potential flow theory and streamline patterns. In the deep water region, the velocities decreased during the compression wave passage and remained positive after the surge passage. In contrast, a transient recirculation occurred in the shallow water zone, being the strongest next to the base of the transverse slope. Dye-injection tests showed a sizeable region where a transient recirculation occurred. The unsteady transverse velocity component was larger next to the bed, in particular close to the joint between the sloped and flat bed, compared to near the free-surface. The magnitudes of local transverse velocities were larger than local longitudinal velocities, at this location in particular. Rapid and large fluctuations of the velocities were observed as the compression wave passed.

Overall, this study shows a complicated three-dimensional unsteady turbulent motion in the trapezoidal channel. Strong recirculation and secondary currents were observed on the transverse slope, albeit for short, transient periods. Further investigations should focus on the effects of different transverse slopes and assess the effects at the transition between different transverse gradients.

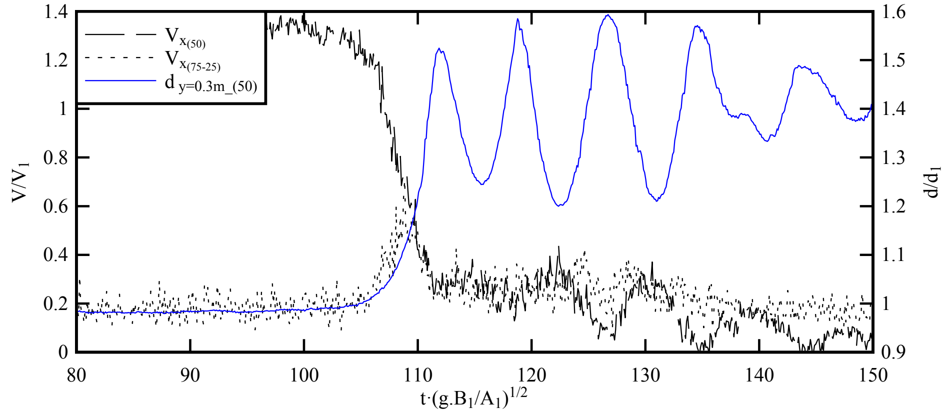

(A) Longitudinal velocity data V_x

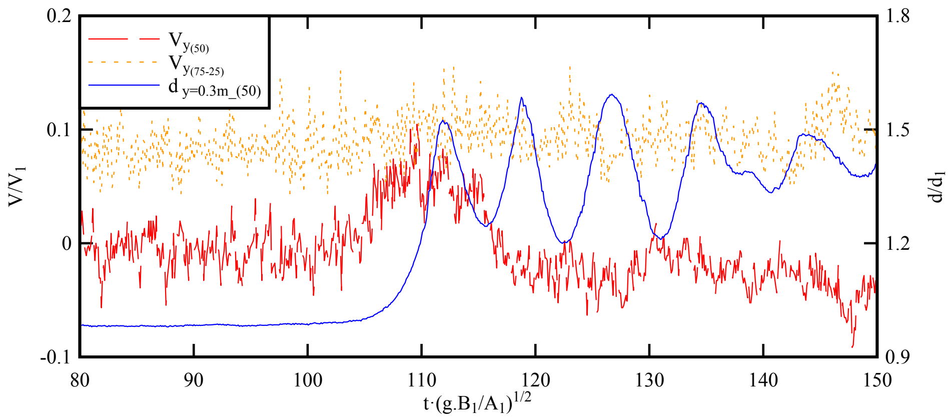

(B) Transverse velocity data V_y

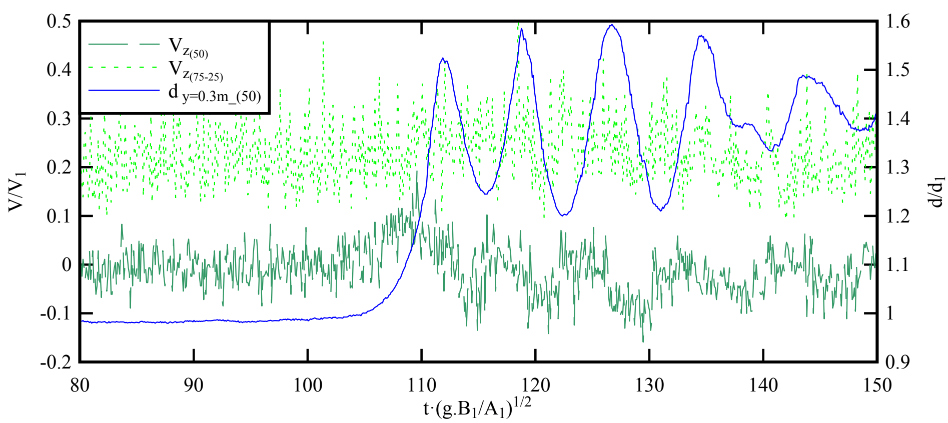

(C) Vertical velocity data V_z

Fig. 8. Time-variations of instantaneous median velocity V_{50}, velocity fluctuations $V_{75\text{-}25} = V_{75} - V_{25}$ and water depth d during the passage of the compression wave - Flow conditions: $Q = 0.054\,m^3/s$, $h = 0.0\,m$, $Fr_1 = 1.4$, $d_1 = 0.151\,m$, $y = 0.3\,m$, $z\text{-}z_{bed} = 0.006\,m$.

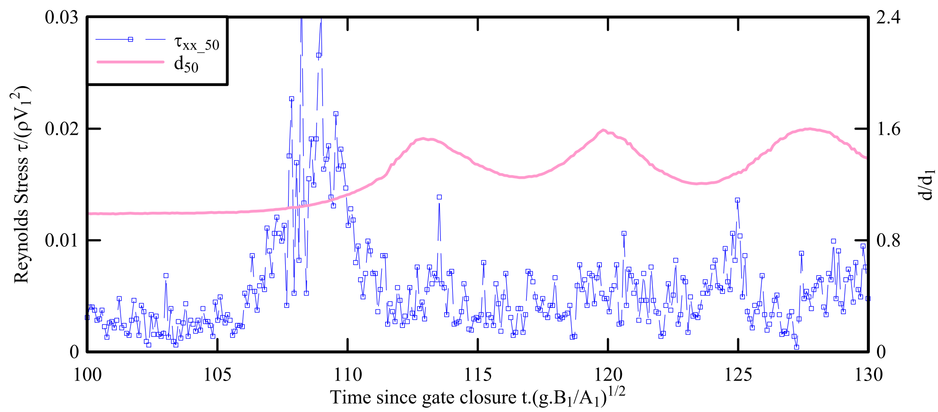

(A) Normal stress τ_{xx}

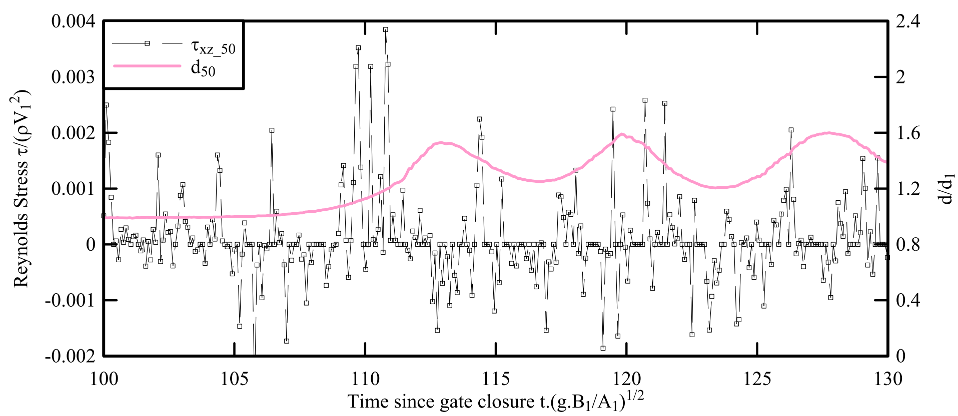

(B) Tangential stress τ_{xz}

Fig. 9. Time-variations of instantaneous ensemble-median Reynolds stress tensor components τ_{xx} and τ_{yz} - - Flow conditions: $Q = 0.054\ m^3/s$, $h = 0.0$ m, $Fr_1 = 1.4$, $d_1 = 0.151$ m, $y = 0.3$ m, $z\text{-}z_{bed} = 0.070$ m.

Declaration of Competing Interest

The authors have no conflict of interest nor vested interest.

Acknowledgements

The authors thank Ms. Urvisha Kiri for her helpful advice, Ms. Ebony Bell for her assistance with some experiments, and Mr. Jason Van Der Gevel and Stewart Matthews (The University of Queensland) for technical assistance.

Appendix A. Application of the momentum equations to a compression wave in non-rectangular asymmetrical channel

A compression wave is as a sudden rise in free-surface elevation constituting a discontinuity of the pressure and velocity fields. In the system of reference following the wave front, the integral form of the equations of conservation of mass and momentum gives a series of relationships between the conjugate flow properties, i.e. in front of and behind the surge front [11,20]:

$$(V_1 + U) \times A_1 = (V_2 + U) \times A_2 \tag{I-1}$$

$$\rho \times (V_1 + U) \times A_1 \times (\beta_1 \times (V_1 + U) - \beta_2 \times (V_2 + U)) = \iint_{A_2} P \times dA - \iint_{A_1} P \times dA + F_{fric} - W_f \times \sin\theta \tag{I-2}$$

where V is the flow velocity and U is the surge celerity for an observer standing on the bank, ρ is the water density, g is the gravity acceleration, A is the channel cross-sectional area measured perpendicular to the main flow direction, β is a momentum correction coefficient, P is the pressure, F_{fric} is the flow resistance force, W_f is the weight force, θ is the angle between the bed slope and horizontal, and the subscripts 1 and 2 refer respectively to the initial flow conditions and the flow conditions immediately after the tidal bore. Note that Eqs. (I-1) and (I-2), as well as the following equations, were developed for a compression wave propagating upstream. A similar reasoning may be expanded for a compression wave travelling downstream.

The above system of equations may provide some analytical solutions within some basic assumptions. Neglecting the flow resistance and the effect of velocity distribution ($\beta_1 = \beta_2 = 1$), and assuming a horizontal channel ($\sin\theta \approx 0$), the momentum equation (I-2) becomes:

$$\rho \times (V_1 + U) \times A_1 \times (V_1 - V_2) = \iint_{A_2} P \times dA - \iint_{A_1} P \times dA \tag{I-3}$$

Assuming a hydrostatic pressure distribution in front of and behind the compression wave, the net pressure force resultant consists of the increase of pressure $\rho \times g \times (d_2 - d_1)$ applied to the initial flow cross-section area A_1 plus the pressure force on the cross-section area $\Delta A = A_2 - A_1$. This latter term equals:

$$\int_{A_1}^{A_2}\int \rho \times g \times (d_2 - z) \times dA = \frac{1}{2} \times \rho \times g \times (d_2 - d_1)^2 \times B' \tag{I-4}$$

where z is the distance normal to the bed, d_1 and d_2 are the flow depths in front of and behind the wave front, and B′ is a characteristic free-surface width. It may be noted that $B_1 < B' < B_2$ where B_1 and B_2 are the upstream and downstream free-surface widths. Another characteristic free-surface width B is defined as:

$$B = \frac{A_2 - A_1}{d_2 - d_1} \tag{I-5}$$

The equation of conservation of mass (I-1) may be expressed as:

$$V_1 - V_2 = (V_1 + U) \times \frac{A_2 - A_1}{A_2} \tag{I-6}$$

The combination of the equations of conservation of mass and momentum yields [3]:

$$Fr_1 = \sqrt{\frac{1}{2} \times \frac{A_2}{A_1} \times \frac{B_1}{B} \times \left(\left(2 - \frac{B'}{B}\right) + \frac{B'}{B} \times \frac{A_2}{A_1}\right)} \tag{I-7}$$

where the Froude number of the compression wave Fr_1 is defined as:

$$Fr_1 = \frac{U + V_1}{\sqrt{g \times \frac{A_1}{B_1}}} \tag{I-8}$$

Eq. (I-10) defines the compression wave Froude number for an irregular channel based upon momentum considerations.

Eq. (I-7) gives an analytical solution of the surge Froude number as a function of the ratios of cross-sectional areas A_2/A_1, and dimensionless characteristic widths B'/B and B_1/B. It may be rewritten to express the ratio of conjugate cross-section areas A_2/A_1 as a function of the upstream Froude number [3]:

$$\frac{A_2}{A_1} = \frac{1}{2} \times \frac{\sqrt{\left(2 - \frac{B'}{B}\right)^2 + 8 \times \frac{\frac{B'}{B}}{\frac{B_1}{B}} \times Fr_1^2} - \left(2 - \frac{B'}{B}\right)}{\frac{B'}{B}} \tag{I-9}$$

which is valid for any positive in an irregular flat channel. The effects of channel cross-sectional shape are taken into account through the ratios B'/B and B_1/B.

In some particular situations, the cross-sectional shape satisfies the approximation $B_2 \approx B \approx B' \approx B_1$: for example, a channel cross-sectional shape with parallel walls next to the waterline or a rectangular channel. A well-know solution of the momentum equation is the Bélanger equation developed for a rectangular horizontal prismatic channel in absence of friction.

Application to an asymmetrical trapezoidal channel

In the present study, the propagation of compression waves was investigated in an asymmetrical non-rectangular channel (Fig. 1). The initial flow cross-section area and free-surface width are:

$$A_1 = \frac{1}{2} \times \lambda \times d_1^2 + W_1 \times d_1 \quad \& \quad B_1 = \lambda \times d_1 + W_1 \quad d_1 < D \tag{I-10a}$$

$$A_1 = d_1 \times W_2 - \lambda \times \frac{D^2}{2} \quad \& \quad B_1 = W_2 \quad d_1 > D \tag{I-10b}$$

where λ^{-1} is transverse slope of the bed (Fig. 1). For this geometry, three boundary conditions may occur depending upon the initial and new (conjugate) flow depths: (a) $d_1 < d_2 < D$, (b) $d_1 < D < d_2$, and (c) $D < d_1 < d_2$. The last case, $D < d_1 < d_2$, is trivial, yielding $B_1 = B = B' = B_2$.

Case $d_1 < d_2 < D$

The analytical solutions of the characteristic widths B and B′ are:

$$B = W_1 + \frac{1}{2} \times \lambda \times (d_1 + d_2) \tag{I-11}$$

$$B' = \frac{d_2^2 \times \left(\frac{1}{2} \times W_1 + \frac{1}{2} \times \lambda \times d_2\right) - d_2 \times d_1 \times \left(W_1 + \frac{1}{2} \times \lambda \times d_1\right) + d_1^2 \times \left(\frac{1}{2} \times W_1 + \frac{1}{3} \times \lambda \times d_1\right)}{\frac{1}{2} \times (d_2 - d_1)^2} \tag{I-12}$$

Case $d_1 < D < d_2$

The analytical solutions of the characteristic widths B and B′ are:

$$B= \frac{W_2 \times d_2 - \frac{\lambda}{2} \times D^2 - d_1 \times \left(W_1 + \frac{\lambda}{2} \times d_1\right)}{d_2 - d_1} \tag{I-13}$$

$$B' = \frac{\frac{\lambda}{6} \times D^3 + \frac{\lambda}{2} \times d_2 \times D \times (d_2 - D) + \frac{1}{2} \times W_1 \times (d_2 - d_1)^2 - \frac{\lambda}{2} \times d_2 \times {d_1}^2 + \frac{\lambda}{3} \times {d_1}^3}{\frac{1}{2} \times (d_2 - d_1)^2} \tag{I-14}$$

Using the method of images, the above solution may be applied to symmetrical trapezoidal channel. In Fig. 1, the vertical line $y = 0$ would be the symmetry line. The resulting symmetrical trapezoidal channel would have a bottom width $2 \times W_1$ with 1V:λH sideslopes.

Appendix B. Movies of compression wave experiments in an asymmetrical trapezoidal channel (digital appendix)

Video-movies of the compression wave experiments were taken using a digital camera Casio™ Exilim Ex10 (120 fps, resolution: 640 px × 480 px). Table A1. describes each video movie available in the digital appendix. The movies were recorded at 120 fps and replayed at 30 fps.

Table A1
Video movies of the compression wave propagation in an asymmetrical trapezoidal channel.

Filename	Camera	Description
CIMG5121.MOV	Casio™ Exilim Ex10 Frame rate: 120 fps	Three-dimensional compression wave propagation at $x = 8.6$ m, viewed looking downstream. Flow conditions: $Q = 0.054$ m^3/s, $S_o = 0.002216$, $Fr_1 = 1.4$, $d_1/D = 1.07$. Movie duration: 17 s
CIMG5228.MOV	Casio™ Exilim Ex10 Frame rate: 120 fps	Three-dimensional compression propagation looking downstream from $x = 7$ m. Flow conditions: $Q = 0.026$ m^3/s, $S_o = 0.002216$, $Fr_1 = 1.32$, $d_1/D = 0.74$. Movie duration: 36 s

Appendix C. Movies of ensemble-median unsteady velocity field beneath compression wave in an asymmetrical trapezoidal channel (digital appendix)

Video movies were developed based upon the instantaneous ensemble-median ADV and Profiler velocity data at $x = 8.6$ m. At each time step, a y-z cross-sectional contour profile was generated, including the no-slip condition at the fixed boundaries. The resultant images were played back in slow motion movies. The ensemble-median velocity data were combined with the ADM data to include the instantaneous transverse surface profile. It is acknowledged that the spacing between sampling points might yield some error in the spatial interpolation throughout the cross section. Practically, the data showed the highest velocity gradient next to the bed in the steady-state and unsteady velocities at the bed. With velocity profiling every millimetre next to the bed, from $z = z_{bed}$ up to 30 mm, the main effects were believed to be captured, including a marked effect of compression wave passage on the vertical velocity gradient, as well as the transverse secondary motion along the inclined (1V:3H) slope.

Each movie started at the steady state, with the solid purple line and cross symbols showing the water surface. The arrival of the compression wave may be seen with the initial raise and following oscillations of the transverse water level. The legend gives the colour coding of the dimensionless velocity component V_i/V_1, with V_1 the initial flow velocity and $i = x$, y or z. Finally the video movies are played at a 1/8th speed of real-time (see Table A2).

Table A2
Video movies of unsteady velocity data beneath compression wave in an asymmetrical trapezoidal channel.

Filename	Velocity component	Description
26_0_Unsteady_Vx_Rev2.avi	V_x	Flow conditions: $Q = 0.026$ m^3/s,
26_0_Unsteady_Vy_Rev2.avi	V_y	$S_o = 0.002216$, $Fr_1 = 1.3$,
26_0_Unsteady_Vz_Rev2.avi	V_z	$d_1/D = 0.74$
54_0_Unsteady_Vx_Rev3.avi	V_x	Flow conditions: $Q = 0.054$ m^3/s,
54_0_Unsteady_Vy_Rev3.avi	V_y	$S_o = 0.002216$, $Fr_1 = 1.4$,
54_0_Unsteady_Vz_Rev3.avi	V_z	$d_1/D = 1.07$

Appendix D. Supplementary material

Supplementary data to this article can be found online at https://doi.org/10.1016/j.expthermflusci.2019.109986.

References

[1] F. Benet, J.A. Cunge, Analysis of experiments on secondary undulations caused by surge waves in trapezoidal channels, J. Hydraul. Res. IAHR 9 (1) (1971) 11–33.

[2] J. Cabonce, R. Fernando, H. Wang, H. Chanson, Using small triangular baffles to facilitate upstream fish passage in standard box culverts, Environ. Fluid Mech. 19 (1) (2019) 157–179, https://doi.org/10.1007/s10652-018-9604-x.

[3] H. Chanson, Momentum considerations in hydraulic jumps and bores, J. Irrigat. Drainage Eng. ASCE 138 (4) (2012) 382–385, https://doi.org/10.1061/(ASCE)IR.1943-4774.0000409.

[4] H. Chanson, D. Reungoat, B. Simon, P. Lubin, High-frequency turbulence and suspended sediment concentration measurements in the garonne river tidal bore, Estuarine Coast. Shelf Sci. 95 (2–3) (2011) 298–306, https://doi.org/10.1016/j.ecss.2011.09.012.

[5] H. Chanson, N.J. Docherty, Turbulent velocity measurements in open channel bores, Eur. J. Mech. B/Fluids 32 (2012) 52–58, https://doi.org/10.1016/j.euromechflu.2011.10.001.

[6] H. Chanson, Y.H. Toi, Physical modelling of breaking tidal bores: comparison with prototype data, J. Hydraul. Res. IAHR 53 (2) (2015) 264–273, https://doi.org/10.1080/00221686.2014.989458.

[7] R.G.A. Craig, C. Loadman, B. Clement, P.J. Ruesello, E. Siegel, Characterization and testing of a new bistatic profiling acoustic doppler velocimeter: the vectrino-II, Proc. IEEE/OES/CWTM 10th Working Conference on Current, Waves and Turbulence Measurement (CWTM), Monterey, Canada, 20–23 March, 2011, pp. 246–252, , https://doi.org/10.1109/CWTM.2011.5759559.

[8] J.A. Cunge, Comparaison des résultats des essais d'intumescences effectués sur le modèle réduit et sur le modèle mathématique du canal Oraison-Manosque, La Houille Blanche (1) (1966) 55–70, https://doi.org/10.1051/lhb/1966003.
[9] H. Favre, Etude Théorique et Expérimentale des Ondes de Translation dans les Canaux Découverts, ('Theoretical and Experimental Study of Travelling Surges in Open Channels.') Dunod, Paris, France, 1935 (in French).
[10] F.B. Gessner, The origin of secondary flow in turbulent flow along a corner, J. Fluid Mech. 58 (Part 1) (1973) 1–25.
[11] F.M. Henderson, Open Channel Flow, MacMillan Company, New York, USA, 1966.
[12] H.G. Hornung, C. Willert, S. Turner, The flow field downstream of a hydraulic jump, J. Fluid Mech. 287 (1995) 299–316.
[13] C. Jaeger, Engineering Fluid Mechanics, Blackie & Son, Glasgow, UK, 1956, p. 529.
[14] C.E. Keevil, H. Chanson, D. Reungoat, Fluid Flow and sediment entrainment in the garonne river bore and tidal bore collision, Earth Surface Process. Landforms 40 (12) (2015) 1574–1586, https://doi.org/10.1002/esp.3735.
[15] U. Kiri, X. Leng, H. Chanson, Positive surge propagation in non-rectangular channels, Proceedings of 13th Hydraulics in Water Engineering Conference HIWE2017, Engineers Australia, Sydney, 13-16 November, 2017, p. 9.
[16] C. Koch, H. Chanson, Turbulence measurements in positive surges and bores, J. Hydraul. Res. IAHR 47 (1) (2009) 29–40, https://doi.org/10.3826/jhr.2009.2954.
[17] X. Leng , Study of Turbulence: the Unsteady Propagation of Bores and Surges, Ph.D. thesis, School of Civil Engineering, The University of Queensland, Brisbane, Australia, 364 pages & 2 Digital Appendices, 2018, doi: 10.14264/uql.2018.501.
[18] X. Leng, H. Chanson, Coupling between free-surface fluctuations, velocity fluctuations and turbulent Reynolds stresses during the upstream propagation of positive surges, bores and compression waves, Environ. Fluid Mech. 16(4) (2016) 695–719 & digital appendix, doi: 10.1007/s10652-015-9438-8.
[19] X. Leng, H. Chanson, Integral turbulent scales in unsteady rapidly varied open channel flows, Exp. Therm. Fluid Sci. 81 (2017) 382–395, https://doi.org/10.1016/j.expthermflusci.2016.09.017.
[20] J.A. Liggett, Fluid Mechanics, McGraw-Hill, New York, USA, 1994.
[21] J.S. Montes, Hydraulics of Open Channel Flow, ASCE Press, New-York, USA, 1998, p. 697.
[22] D. Naot, W. Rodi, Calculation of secondary currents in channel flow, J. Hydraul. Div. ASCE 108 (HY8) (1982) 948–967.
[23] D.Z. Pan, H. Chanson, Physical modelling of tidal bore dyke overtopping: implication on individuals' safety, Proc. 36th IAHR World Congress, The Hague, The Netherlands, 27 June-3 July, Theme 4, 2015, pp. 3824–3831.
[24] A. Preissmann, J.A. Cunge, Low-amplitude undulating hydraulic jump in trapezoidal canals, J. Hydraul. Res. IAHR 5 (4) (1967) 263–279.
[25] D. Reungoat, P. Lubin, X. Leng, H. Chanson, Tidal bore hydrodynamics and sediment processes: 2010–2016 field observations in France, Coast. Eng. J. 60 (4) (2018) 484–498, https://doi.org/10.1080/21664250.2018.1529265.
[26] J.A. Sandover, C. Taylor, Cnoidal waves and bores, J. La Houille Blanche (1962) 443–445.
[27] J.J. Stoker, Water Waves. The mathematical Theory with Applications, Interscience Publishers, New York, USA, 1957, p. 567.
[28] S. Sun, X. Leng, H. Chanson, Rapid operation of a Tainter gate: generation process and initial upstream surge motion, Environ. Fluid Mech. 16 (1) (2016) 87–100, https://doi.org/10.1007/s10652-015-9414-3.
[29] R.E. Thomas, L. Schindfessel, S.J. Mclelland, S. Creelle, T. De Mulder, Bias in mean velocities and noise in variances and covariances measured using a multistatic acoustic profiler: the Nortek Vectrino Profiler, Meas. Sci. Technol. 28 (2017) 25, https://doi.org/10.1088/1361-6501/aa727 Paper 075302.
[30] A. Treske, Undular bores (favre-waves) in open channels - experimental studies, J. Hydraul. Res. 32 (3) (1994) 355–370, https://doi.org/10.1080/00221689409498738.